



Science Arts & Métiers (SAM)

is an open access repository that collects the work of Arts et Métiers Institute of Technology researchers and makes it freely available over the web where possible.

This is an author-deposited version published in: <https://sam.ensam.eu>
Handle ID: <http://hdl.handle.net/10985/8224>

To cite this version :

Yun-Mei LUO, Luc CHEVALIER, Françoise UTHEZA, Eric MONTEIRO - Numerical Simulation of the Thermodependant Viscohyperelastic Behavior of Polyethylene Terephthalate Near the Glass Transition Temperature: Prediction of the Self-Heating During Biaxial Tension Test - Polymer Engineering and Science - Vol. 53, p.2683-2695 - 2013

Any correspondence concerning this service should be sent to the repository

Administrator : scienceouverte@ensam.eu



Numerical Simulation of the Thermodependant Viscohyperelastic Behavior of Polyethylene Terephthalate Near the Glass Transition Temperature: Prediction of the Self-Heating During Biaxial Tension Test

Yun-Mei Luo,¹ Luc Chevalier,¹ Françoise Utheza,¹ Eric Monteiro²

¹ Université Paris-Est, Laboratoire Modélisation et Simulation Multi Echelle, MSME UMR 8208, CNRS, 5 Bd Descartes, 77454 Marne-la-Vallée CEDEX 2, France

² Laboratoire Procédés et Ingénierie en Mécanique et Matériaux (PIMM, UMR CNRS 8006), Arts et Métiers ParisTech, 151 boulevard de l'Hôpital, 75013 Paris, France

The poly ethylene terephthalate near the glass transition temperature highlights a strongly non linear elastic and viscous behaviour when biaxially stretched at high strain rates representative of the injection stretch blow moulding process. A non linear visco-hyperelastic model, where characteristics are coupled to the temperature, has already been identified from equi-biaxial tension experimental results. The weak form of the mechanical part of the model is presented and implemented into a finite element code developed in the Matlab environment and validated by comparing numerical simulation of equi-biaxial testing with the analytical solution in the isothermal case. Considering the thermal aspects, an experimental study, where PET sheets are heated using infrared (IR for short) lamps is also presented. The modeling of the IR radiation of the sheet helps to identify the thermal properties of the PET. The thermal model is then implemented in the finite element code, coupled to the 2D viscoelastic model. A discussion is made to justify the accuracy of the assumption made on homogeneity of the temperature field through the thickness. The simulation of the 2D plane stress equibiaxial test shows the important influence of the thermal aspects and the coupled thermo-mechanical software is used to quantify the self-heating phenomenon in the case of the biaxial elongations of PET sheets at high strain rates. POLYM. ENG. SCI., 53:2683–2695, 2013. © 2013 Society of Plastics Engineers

INTRODUCTION

The injection stretch blow molding (ISBM) process that is managed at a temperature near or slightly above the glass transition temperature (T_g) involves multiaxial large strains at high strain rate of the polyethylene tereph-

thalate (PET) material. The performance of a PET bottles produced by the ISBM process depends on many parameters. During the ISBM process, the PET behavior exhibits a highly elasticity, a strain hardening effect, and a strong viscous and temperature dependency. Therefore, many researches have been conducted on the rheological behavior of PET: Marckmann et al. [1] proposed and used a hyperelastic modeling approach which could not take into account the strain rate effect. Gorlier et al. [2, 3] also used the hyperelastic type models, however, although these models have demonstrated some success in representing the PET behavior at specific strain rates, they have been found to be unstable in the numerical simulation. Chevalier and Marco [4] have managed biaxial tension tests near T_g with a range of strain rates from 0.02 to 2 s⁻¹. They proposed a simple viscoplastic model [4] identified from these tension tests. This model has been used by Bordival et al. [5] in a numerical procedure based on simulations of the heating and blowing phases performed to optimize the stretch blow molding process. Cosson et al. [6], then developed this viscoplastic model into an anisotropic version. The strain hardening effect observed during tension can be related with the strain induced modifications of the microstructure of PET but this viscoplastic model approach fails to represent the relaxation stage after tension which Chevalier and Marco [7] carried out from the relaxation tests. In their work, the relaxation time has been identified from these tests and clearly demonstrates the contribution of a viscous part in a highly elastic macromolecular network. This stress relaxation behavior is the main characteristics associated with viscoelastic materials. Therefore, the viscoelastic model which take into account the strain hardening and strain rate effects have been used for ISBM process [8, 9]. However,

the classical viscoelastic models such as the Upper Convected Maxwell model [9] or the Giesekus model [10] do not adequately demonstrate the strain hardening effect. Buckley and Jones [11, 12] proposed a nonlinear viscoelastic model which is physically based on molecular network theory. Lately, Menary et al. [13] have examined three different constitutive models: hyperelastic model, creep model and a viscoelastic model (Buckley model) in the ISBM simulation using the finite element package ABAQUS/standard. They found that the Buckley model (viscoelastic model) gave a better result than the others two models in terms of predicting thickness distribution in the bottle. Inspired from Figiel and Buckley's work [14], Chevalier et al. [15, 16] have recently proposed a nonlinear incompressible viscohyperelastic model to represent the complex constitutive behavior of PET. Experimental uniaxial and biaxial tests performed on PET were carried out by Menary et al. [17] in Queen's University of Belfast. These tension tests were managed with various tension speeds (from 1 to 32 s⁻¹), which are higher than in Chevalier and Marco's work [4]. The nonlinear forms of elastic and viscous characteristics were proposed. Here, we implement this complex viscohyperelastic model into a finite element code in the Matlab environment. The weak form of this four-field model (velocity \underline{V} , the elastic left Cauchy Green tensor \underline{B}_e , and the related pressure p and q for the incompressibility assumptions) is presented in the two dimensional (2D) specific plane stress case. It enables to reduce the number of field to 2 (velocity, the elastic left Cauchy Green tensor). Simulations of biaxial tests are managed to compare with the analytical solution in the isothermal conditions.

Effects of temperature, initial heating conditions or self-heating during the process, are of fundamental importance during the ISBM process of PET bottles. In the ISBM process, an initial preform is heated in an oven to the process temperature, which is near or slightly above T_g . Over this temperature T_g , the mobility of the molecular chains in material PET affects the orientation and the microstructure (crystallization). The mechanical properties of PET are dependent on the microstructural morphology of the PET and strongly depend on the process temperature as well as on the strain rates. On the other hand, the low mobility of micromolecules and the high viscosity of the material generate dissipation of energy which leads to a self-heating phenomenon. This self-heating effect must be taken into account in the simulation. In contrast, many existing numerical studies of ISBM [14, 18] neglect heat transfer: the temperature has been assumed to be constant during the process and the deformation induced heat was neglected. These researches show that a numerical simulation neglecting the effect of temperature during stretch-blow molding process could not accurately predict or model the orientation and crystallization, which are highly temperature dependent during the process. Therefore, it is essential to incorporate heat transfer to represent the mechanical properties of the final bottles. Schmidt et al. [19] developed their work [8] in ISBM simulation by devel-

oping a nonisothermal finite element simulation to embed heat transfer during the deformation process. However, it did not show the significant improvement in terms of predicting thickness distribution and the force exerted by the stretch rod. Yang et al. [20, 21] continued the work of Menary et al. [13] in a 2D isothermal simulation to a 2D nonisothermal simulation by using the Buckley model to represent the PET behavior. Significant nonlinear differentials have been found in temperature and strain in the bottle thickness. Here, we first identify the thermal properties from infrared (IR) heating tests of PET sheets. The identified parameters are compared to classical values of the literature. Especially, the IR heating flux coming from IR lamps is studied using radiative laws adapted to the test geometry. A good correlation is discovered. Then, the thermal part coupled with the viscohyperelastic model for the mechanical part is used to perform the simulation. The simulation enables to quantify the self-heating during the biaxial tests.

In the first section of this work, we present the implementation of the proposed nonlinear incompressible viscohyperelastic model into a finite element code developed with Matlab. We present a two-field finite element formulation: global velocity \underline{V} and elastic Cauchy Green tensor \underline{B}_e . Rectangular finite elements with quadratic and linear interpolations are used for velocity and elastic left Cauchy Green tensor. A numerical simulation of 2D plane stress case is performed. It reproduces well the strain hardening effect.

In the second section, a procedure is proposed for the identification of the thermal parameters from experimental results of a test where PET sheets are heated using IR lamps. Sheets used in this study are made with the PET Arnite D00301 from DSM industries. The IR heating with IR camera is widely used in the experimental setup for the heat transfer [22, 23]. The Monte Carlo method is used to identify the parameters from the temperature evolution measured on the front face (in regard of the lamps) and the rear face of the sheet. The heat capacity, C_p , is considered as a function of the temperature while the other parameters (thermal conductivity, emissivity, convection coefficient, etc.) are assumed to be independent of the temperature. A large section is devoted to the comparison of the identified parameters with classical values of the literature, especially for the IR heating modeling. Moreover, the weak form describing thermal behavior adapted to plane stress case is presented in the end of this section.

In the third section, to accurately simulate the ISBM process, the thermal and mechanical parts are put together. Nonlinear mechanical and thermal equilibrium equations are solved with implicit schemes on the current deformed configuration, which is updated at each time step. Finally, the parameters identified in the proposed model have to be adjusted because the self-heating effect is not negligible and has an important effect on the viscous part of the model. Therefore, an optimization procedure is managed to adjust the characteristics of the PET for these viscohyperelastic model expressions to represent conveniently the biaxial experimental tension tests [17].

NUMERICAL SIMULATION OF THE MODEL IN PLANE STRESS CASE

Model Presentation

Inspired from Figiel and Buckley [14], we proposed in Refs. [15, 16], a nonlinear incompressible viscohyperelastic model for both elastic and viscous parts to represent the mechanical behavior. To represent the strain hardening and strain rate effect and temperature dependency, we choose two rheological functions for elastic and viscous parts: $G(\varepsilon_e)$ and $\eta(\varepsilon_v, \dot{\varepsilon}_v, T)$.

$$\begin{cases} \hat{\underline{\underline{\sigma}}} = 2G(\varepsilon_e)\hat{\underline{\underline{\varepsilon}}}_e \\ \hat{\underline{\underline{\sigma}}} = 2\eta(\varepsilon_v, \dot{\varepsilon}_v, T)\underline{\underline{D}}_v \end{cases} \text{ and } \underline{\underline{\sigma}} = 2\eta_N\underline{\underline{D}} + \hat{\underline{\underline{\sigma}}} - p\underline{\underline{I}} - q\underline{\underline{I}} \quad (1)$$

where $\underline{\underline{\sigma}}$ is the Cauchy stress tensor, $\underline{\underline{D}}_v$ is the symmetric part of the viscous velocity gradient, $\underline{\underline{D}}$ is the symmetric part of the global velocity gradient, $\underline{\underline{I}}$ is the identity matrix, ε_e is the equivalent elastic strain, ε_v is the equivalent viscous strain, $\dot{\varepsilon}_v$ is the equivalent viscous strain rate, T is the temperature, the subscript “ \wedge ” denotes the deviatoric part of the tensor, η_N is the small value of the viscosity of the Newtonian branch of the Zener-like model used to solve the ill-conditioned problem, and ε_e is the elastic part of the Eulerian strain measure defined by:

$$\underline{\underline{\varepsilon}}_e = \frac{1}{2}(\underline{\underline{B}}_e - \underline{\underline{I}}) \quad (2)$$

where $\underline{\underline{B}}_e$ is the elastic left Cauchy Green tensor. p is a Lagrange multiplier associated to the global incompressibility condition, and q is the multiplier associated to the incompressibility of the elastic part. Since the elastic and global parts are incompressible, the viscous part is supposed to be also incompressible:

$$\det \underline{\underline{B}}_e = 1, \quad \text{div} \bar{\underline{\underline{V}}} = \text{trace} \underline{\underline{D}} = 0, \quad \text{div} \bar{\underline{\underline{V}}}_v = \text{trace} \underline{\underline{D}}_v = 0 \quad (3)$$

where $\bar{\underline{\underline{V}}}$ is the global velocity and $\bar{\underline{\underline{V}}}_v$ is the viscous velocity.

The assumption of an additive decomposition of elastic and viscous velocity gradient is adopted to describe the kinematic structure of this model:

$$\underline{\underline{D}} = \underline{\underline{D}}_e + \underline{\underline{D}}_v \quad (4)$$

where $\underline{\underline{D}}_e$ is the symmetric part of the elastic velocity gradient.

Combining Eqs. 1, 2, and 4 in the Oldroyd derivation of the elastic left Cauchy Green tensor leads to:

$$\frac{\delta \underline{\underline{B}}_e}{\delta t} + \frac{G}{\eta} \underline{\underline{B}}_e \cdot \hat{\underline{\underline{B}}}_e = 0 \quad (5a)$$

TABLE 1. The numerical value of G_0 .

Strain rate (s^{-1})	1	2	4	8	16
G_0 (MPa)	7.2	8.1	7.7	7.9	8.9
Min G_0 (MPa)	7.2				
Max G_0 (MPa)	8.9				

where G is the elastic shear modulus, η is the viscosity and the Oldroyd derivation $\delta \underline{\underline{B}}_e / \delta t$ is defined by:

$$\frac{\delta \underline{\underline{B}}_e}{\delta t} = \underline{\underline{B}}_e + \underline{\underline{B}}_e \underline{\underline{\Omega}} - \underline{\underline{\Omega}} \underline{\underline{B}}_e - a(\underline{\underline{B}}_e \underline{\underline{D}} + \underline{\underline{D}} \underline{\underline{B}}_e) \text{ with } a = 1 \quad (5b)$$

where is $\underline{\underline{\Omega}}$ the global spin.

Identification of the Material's Properties

Both the elastic and the viscous parts of the model must contribute to the strain rate effect. We first focus on the elastic part. One can identify the initial shear modulus G_0 from the initial slope of the global experimental strain–stress curves which were carried out by Menary et al. [17], because there is no viscous strain at the very beginning of the test. Table 1 show that G_0 does not vary much from one strain rate to another.

As the biaxial tests are conducted at constant nominal strain rate, the global strain rate decreases versus time. If the shear modulus G remains constant, it leads to a contradiction because the viscous strain rate may become negative. Therefore, we consider a Hart-Smith-like model to represent the elastic part:

$$G(\varepsilon_e) = G_0 \exp(\Lambda(I_1 - 3)^2), \quad I_1 = \text{trace}(\underline{\underline{B}}_e) \quad (6)$$

where Λ is a dimensionless parameter.

For the nonlinear viscous part of the model, we follow the same method as in Cosson et al. [6] to represent macroscopically the strain hardening effect, but we choose a Carreau type law instead of the power law to describe the influence of the strain rate:

$$\eta(\varepsilon_v, \dot{\varepsilon}_v, T) = \eta_0 h(\bar{\varepsilon}_v) f(\bar{\varepsilon}_v) \quad (7)$$

$$\text{with } f(\bar{\varepsilon}_v) = \frac{1}{(1 + (\lambda(\bar{\varepsilon}_v / \dot{\varepsilon}_{\text{ref}}))^a)^{(1-m)/a}} \quad (8)$$

where λ , m , and a are parameters in the Carreau type law and $\dot{\varepsilon}_{\text{ref}}$ is a reference strain rate that can be taken equal to 1 s^{-1} for sake of simplicity. The strain hardening effect is related to the h function which increases continuously with $\bar{\varepsilon}_v$. We detailed the identification procedure for the h function in [15, 16], here we slightly changed the form of the function. Since the strain hardening effect is influenced by the temperature, h is a function of T too:

$$\eta_0 h(\bar{\varepsilon}_v, T) = \frac{\eta_0(T) \cdot (1 - \exp(-K\bar{\varepsilon}_v))}{(1 - (\bar{\varepsilon}_v / \varepsilon_{v \text{ lim}}(T)))^N} \quad (9)$$

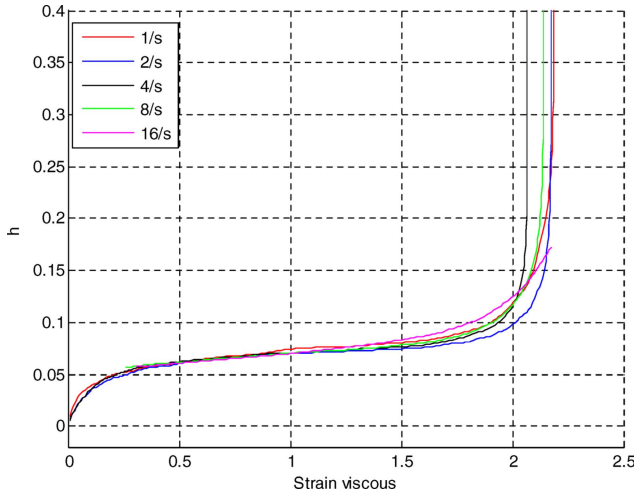


FIG. 1. The h evolution versus the equivalent viscous strain $\bar{\varepsilon}_v$ when $m = 0.25$ [15, 16]. [Color figure can be viewed in the online issue, which is available at wileyonlinelibrary.com.]

According to the form of the lines of h showed in Fig. 1, we propose the function in Eq. 9, where η_0 is related to the level of the function on the ‘plateau’, K is a constant related to the initial slope of the curve, $\varepsilon_{v\text{lim}}$ is the strain value corresponding to the vertical asymptote of the h curve and N an exponent that fits the “beginning” of the quick increase in the curve.

Parameters K and N do not vary much with the temperature; at the contrary, variables $\eta_0(T)$ and $\varepsilon_{v\text{lim}}(T)$ show a significant dependence on temperature. We choose the Williams–Landel–Ferry (WLF) model for the evolution of $\eta_0(T)$:

$$\ln(a_T) = \frac{-C_1(T - T_{\text{ref}})}{C_2 + T - T_{\text{ref}}}, \eta_0(T) = a_T \eta_0(T_{\text{ref}}) \quad (10)$$

where C_1 and C_2 are the WLF parameters, $T_{\text{ref}} = 90^\circ\text{C}$. We propose the evolution of $\varepsilon_{v\text{lim}}(T)$ in the following way:

$$\varepsilon_{v\text{lim}} = \varepsilon_{v\text{lim_ref}} \left(1 + \frac{B_1(T_{\text{ref}} - T)}{(T - B_2)} \right) \quad (11)$$

where $\varepsilon_{v\text{lim_ref}} = \varepsilon_{v\text{lim_}90^\circ\text{C}}$. Finally, the characteristics of the PET for these viscohyperelastic model expressions to represent conveniently the experimental are listed in Table 2.

TABLE 2. The characteristics of the PET.

$G_0 = 8 \text{ MPa}$	$\eta_0 = 8.4 \text{ MPa}\cdot\text{s}$	$C_1 = 1.88$
$\Lambda = 0.001$	$K = 3.2$	$C_2 = 25.81^\circ\text{C}$
$\lambda = 9.91$	$h_0 = -0.21$	$B_1 = 0.07$
$a = 2$	$N = 0.42$	$B_2 = 111.88^\circ\text{C}$
$m = 0.2$	$\varepsilon_{v\text{lim_ref}} = 1.83$	

Weak Form of the Plane Stress 2D Viscohyperelastic Problem

In the equibiaxial elongation plane stress case, before deriving the weak form, we can establish a relation between the pressures, the velocity, and the elastic left Cauchy Green tensor:

$$\begin{aligned} \sigma_{33} = 0 &\Rightarrow p + q \\ &= -2\eta_N(D_{11} + D_{22}) \\ &+ \frac{G(\varepsilon_e)}{3} \left(\frac{2}{B_{e11}B_{e22} - B_{e12}^2} - B_{e11} - B_{e22} \right). \end{aligned} \quad (12)$$

The viscohyperelastic model is implemented in the Matlab environment using a finite element approach. A two fields (global velocity V and the elastic left Cauchy Green tensor $\underline{\underline{B}}_e$) variational formulation is proposed for plane stress incompressible problem. Some manipulations of Eqs. 5, 6, and 12 lead to the following weak form:

$$\begin{aligned} R_V &= 2\eta_N \int_{\Omega} \underline{\underline{D}}^* : \underline{\underline{D}} d\Omega + G \int_{\Omega} \underline{\underline{D}}^* : \underline{\underline{B}}_e d\Omega + 2\eta_N \\ &\int_{\Omega} \underline{\underline{D}}^* : \underline{\underline{I}}(D_{11} + D_{22}) d\Omega \\ &- \frac{G}{3} \int_{\Omega} \underline{\underline{D}}^* : \underline{\underline{I}} \frac{1}{B_{e11}B_{e22} - B_{e12}^2} d\Omega - \int_{\partial\Omega_F} \underline{\underline{V}}^* \underline{\underline{F}}^d dS = 0; \\ R_{B_e} &= \int_{\Omega} \underline{\underline{B}}_e^* : \left(\frac{\delta \underline{\underline{B}}_e}{\delta t} + \frac{G(\varepsilon_e)}{\eta(\varepsilon_v, \bar{\varepsilon}_v, T)} \underline{\underline{B}}_e \hat{\underline{\underline{B}}}_e \right) d\Omega = 0 \end{aligned} \quad (13)$$

where the superscript $*$ designates test quantities and $\underline{\underline{F}}^d$ the prescribed traction field over the boundary $\partial\Omega_F$ where the loads are imposed. The integral equations are studied on the entire volume Ω .

This strongly nonlinear problem (finite elastic displacements, elastic left Cauchy Green tensor $\underline{\underline{B}}_e$, nonconstant shear modulus G , and viscosity η) is solved using a classical Newton–Raphson iterative procedure. The consistent linearization must be done with Gâteaux operators and the linear form of the problem for the increment ΔV and $\Delta \underline{\underline{B}}_e$ is written in the following system:

$$\begin{bmatrix} [D_{\Delta V}\{R_V\}] & [D_{\Delta B_e}\{R_V\}] \\ [D_{\Delta V}\{R_{B_e}\}] & [D_{\Delta B_e}\{R_{B_e}\}] \end{bmatrix} \begin{Bmatrix} [\Delta V] \\ [\Delta \underline{\underline{B}}_e] \end{Bmatrix} = - \begin{Bmatrix} [R_V] \\ [R_{B_e}] \end{Bmatrix} \quad (14)$$

where $D_{\Delta V}\{R_V\}$, $D_{\Delta B_e}\{R_V\}$, $D_{\Delta V}\{R_{B_e}\}$, and $D_{\Delta B_e}\{R_{B_e}\}$ are the Gâteaux derivatives related to the increments:

$$\begin{aligned} D_{\Delta V}\{R_V\} &= 2\eta_N \int_{\Omega} \underline{\underline{D}}^* : \underline{\underline{D}}(\Delta V) d\Omega + 2\eta_N \\ &\int_{\Omega} \underline{\underline{D}}^* : \left(\left(\underline{\underline{D}}(\Delta V) : \underline{\underline{I}} \right) \underline{\underline{I}} \right) d\Omega \end{aligned}$$

$$\begin{aligned}
D_{\Delta B_e}\{R_V\} &= \int_{\Omega} \underline{\underline{D}}^* : (G(\varepsilon_e) \Delta \underline{\underline{B}}_e) d\Omega \\
&\quad - \int_{\Omega} \underline{\underline{D}}^* : \left(G(\varepsilon_e) \frac{1}{\Delta B_{e11} \Delta B_{e22} - \Delta B_{e12}^2} \underline{\underline{I}} \right) d\Omega \\
&\quad - \int_{\Omega} \underline{\underline{D}}^* : (D_{\Delta B_e}\{G(\varepsilon_e)\} \underline{\underline{B}}_e) d\Omega \\
&\quad - \int_{\Omega} \underline{\underline{D}}^* : \left(\frac{1}{B_{e11} B_{e22} - B_{e12}^2} D_{\Delta B_e}\{G(\varepsilon_e)\} \underline{\underline{I}} \right) d\Omega \\
D_{\Delta V}\{R_{B_e}\} &= 2 \int_{\Omega} \underline{\underline{B}}_e^* : (\underline{\underline{B}}_e \Omega(\Delta V)) d\Omega \\
&\quad - 2 \int_{\Omega} \underline{\underline{B}}_e^* : (\underline{\underline{B}}_e D(\Delta V)) d\Omega \\
D_{\Delta B_e}\{R_{B_e}\} &= \int_{\Omega} \underline{\underline{B}}_e^* : \Delta \underline{\underline{B}}_e d\Omega - 2 \int_{\Omega} \underline{\underline{B}}_e^* : (\underline{\underline{\Omega}} \Delta \underline{\underline{B}}_e) d\Omega - 2 \\
&\quad \int_{\Omega} \underline{\underline{B}}_e^* : (\underline{\underline{D}} \Delta \underline{\underline{B}}_e) d\Omega \\
&\quad + \int_{\Omega} \underline{\underline{B}}_e^* : \left(\frac{G(\varepsilon_e)}{\eta(\varepsilon_v, \dot{\varepsilon}_v, T)} \underline{\underline{B}}_e \hat{\Delta} \underline{\underline{B}}_e \right) d\Omega \\
&\quad + \int_{\Omega} \underline{\underline{B}}_e^* : \left(\frac{G(\varepsilon_e)}{\eta(\varepsilon_v, \dot{\varepsilon}_v, T)} \hat{\underline{\underline{B}}}_e \Delta \underline{\underline{B}}_e \right) d\Omega \\
&\quad + \int_{\Omega} \underline{\underline{B}}_e^* : \left(D_{\Delta B_e} \left\{ \frac{G(\varepsilon_e)}{\eta(\varepsilon_v, \dot{\varepsilon}_v, T)} \right\} \underline{\underline{B}}_e \hat{\Delta} \underline{\underline{B}}_e \right) d\Omega
\end{aligned} \tag{15}$$

Figure 2 shows the geometry of the PET specimen during the tension tests, boundary conditions on symmetry axis and the load applied on the edge of the sheet. The PET sheet is submitted to a velocity V on X -axis and

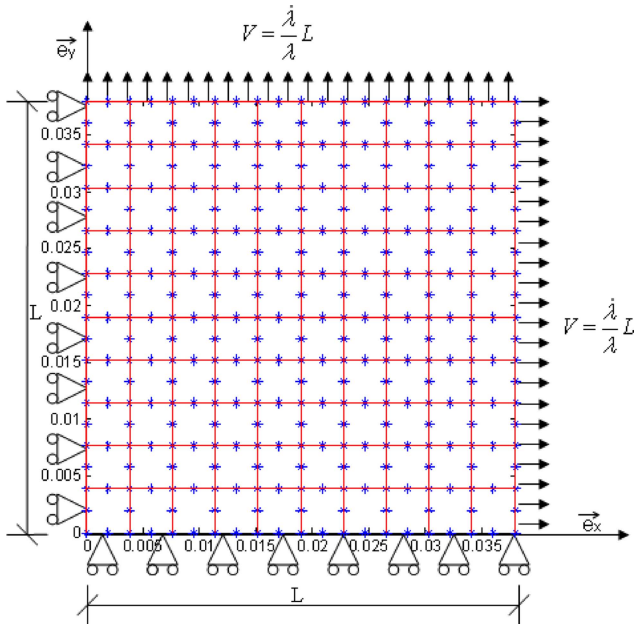


FIG. 2. The 2D rectangular domain with the boundary conditions. [Color figure can be viewed in the online issue, which is available at wileyonlinelibrary.com.]

Y -axis. This case represents the equal biaxial tension case: $\sigma_{xx} = \sigma_{yy}$. According to the axis of symmetry, the equal biaxial tension case can be simulated using one-quarter of the specimen. To compare the experimental results, the length and width of the 2D domain simulated are 38 mm and the thickness is 1.5 mm, which is representative of the PET specimen size (76 mm \times 76 mm \times 1.5 mm) of the test [17].

As showed in Fig. 2, the domain Ω is discretized by a set of eight-node isoparametric rectangles elements. The simulation is managed for different elongation rate $\dot{\lambda}$ obtained from the derivative of stretch ratio λ with respect to time t : so $\dot{\varepsilon} = \dot{\lambda}/\lambda$, $\dot{\varepsilon}$ varies from 1 to 32 s^{-1} .

Simulation the Biaxial Plane Stress Testing

In the case of the classical incompressible problem with a mixed velocity-pressure formulation, the finite ele-

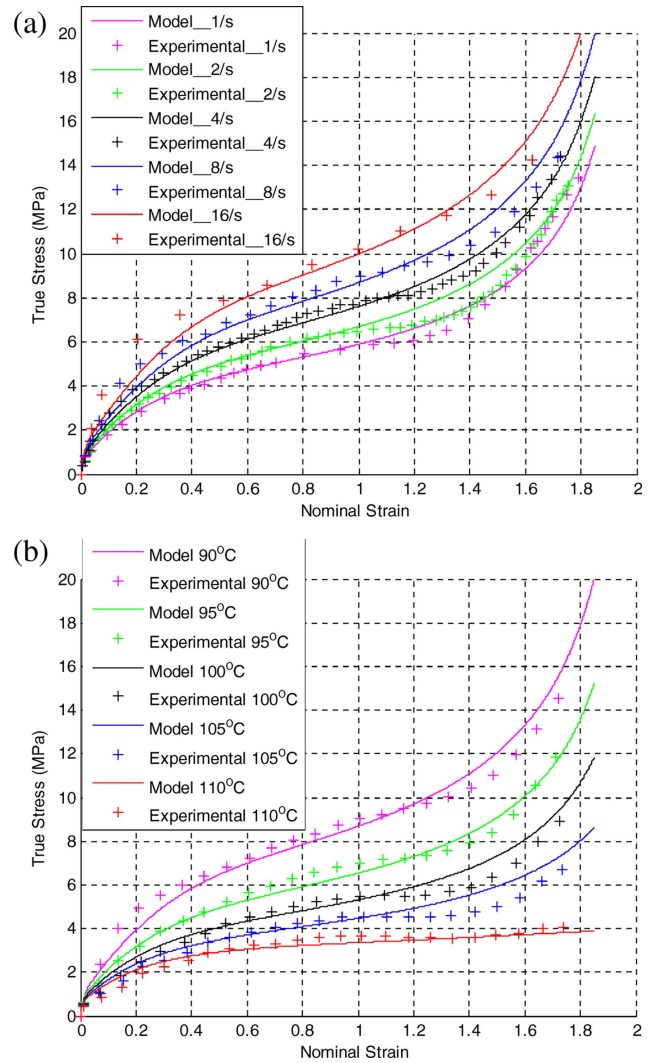


FIG. 3. (a) The experimental data (+) and the finite elements results of the viscoelastic model (lines) at 90°C under different strain rates; (b) the experimental data (+) and the finite elements results of the viscoelastic model (lines) at 8 s^{-1} under different temperatures. [Color figure can be viewed in the online issue, which is available at wileyonlinelibrary.com.]

ment calculations can lead to locking problem if velocity and pressure spaces are not chosen carefully. To be stable, a mixed formulation must verify consistency. The well-known inf-sup condition or the Ladyzenskaia-Babushka-Brezzi (LBB) condition [24] guaranties the stability of a finite element velocity-pressure calculation as a quadratic interpolation for velocity and linear for pressure. By analogy, we choose a quadratic interpolation for velocity \underline{V} and linear interpolation for \underline{B}_e .

The finite elements result matches perfectly with the analytic results. Figure 3a and b shows a substantially good representation of the experimental results. The mean difference does not exceed 10%.

NUMERICAL SIMULATION OF A THERMOMECHANICAL MODEL

Experimental Procedure

Mechanical properties of polymer are strongly influenced by small variation of temperature. On the other hand, the high viscosity of polymers generates important dissipation that impacts the temperature evolutions. Consequently, thermal properties are to be taken into account in the ISBM modeling to achieve accurate simulation of the process. It is necessary to:

- define accurately the initial temperature distribution of the preform at the beginning of the blowing operation;
- identify the thermal properties of the PET to model the behavior law of PET coupled to the thermal laws;
- provide, by coupling the thermal equations with the mechanical equations, the history of the temperature field during the simulation.

In the following, a procedure is proposed for the identification of the thermal parameters. According to Fig. 4, the experimental apparatus which consists in measuring, by thermal imaging, a PET sheet heating by IR lamps. A FLIR B250 IR camera with the wavelength range 7.5–13 μm is used to evaluate the surface temperature distribution. The surface dimension of the 1 mm thickness sheet is 60 mm \times 125 mm. Sheets used in this study are injected from the PET Arnite D00301 following DSM industries recommendations.

We have tested three different distances between the lamps and the PET sheet: 11 cm, 12 cm, and 13 cm. The thermal properties are identified for each distance: we can ensure the values of the heat conductivity, the specific masse, the heat capacity and the convective heat transfer parameters. Moreover, the relation between the heating flux and the distance can be estimated. For a constant heating IR flux, we can notice that the temperature decreases while this distance increases. This is a logical result because the intensity of the radiation decreases when the distance increases [25].

Identification of the Thermal Properties

The software FLIR quick report is used to measure accurately the temperature. In the work of Schmidt et al. [26], they have found that the polymer material is opaque under the wavelength in the range of 8–12 μm . This range matches the one of the IR camera so the PET may be considered like an opaque medium. The black paint used is assumed to be opaque which means that only the radiation emitted from the PET sheet surface is captured by the camera's sensor. To evaluate the temperature field from the IR camera, we need the emissivity value of the PET sheet. However, because we are not able to quantify it precisely, the identification is managed from thermocouple measures. From thermal imaging by camera, the temperature field visualization shows that some temperature heterogeneities only appear on the edges of the sheet surface. According to these results, we can assume that the temperature is homogeneous in the plane of the sheet and only varies in the thickness direction. Therefore, the identification can be done from a 1D model.

The heat transfer equation in the 1D case with the radiative source term can be written in the following way:

$$\rho C_p(T)\dot{T} - k \frac{\partial^2 T}{\partial z^2} = -\text{div}(\vec{q}_r) \quad (16)$$

where ρ the specific mass, C_p the specific heat capacity, k the material's conductivity and \vec{q}_r is the internal radiative heat flux.

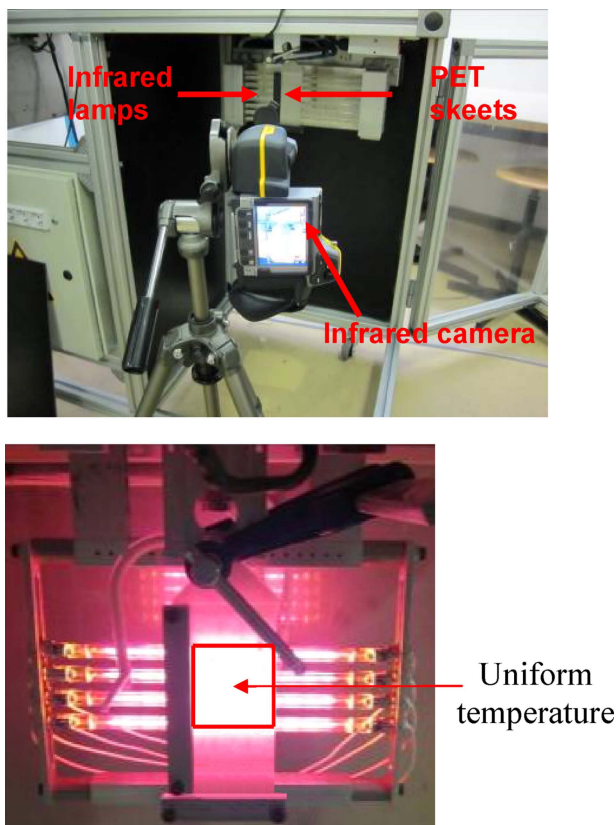


FIG. 4. (a) Experimental heating setup; (b) IR lamps and PET sheet. [Color figure can be viewed in the online issue, which is available at wileyonlinelibrary.com.]

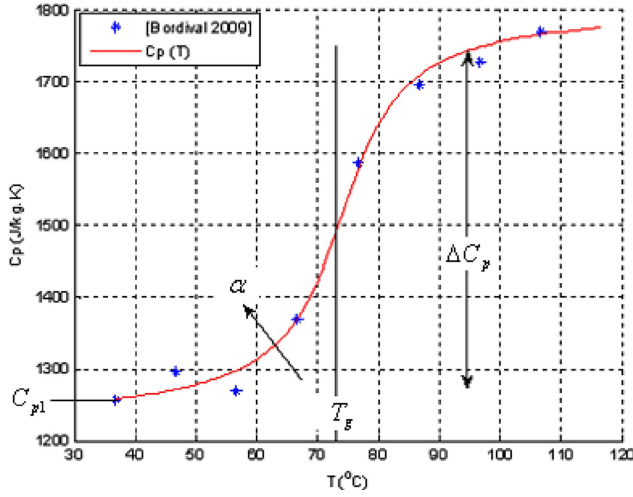


FIG. 5. Heat capacity C_p versus the temperature and the illustration of the C_p function. [Color figure can be viewed in the online issue, which is available at wileyonlinelibrary.com.]

In Cosson et al. [27], the convective heat transfer coefficient for the face in front is little larger than the one on the rear face, but in other works [28], it is the opposite. Therefore, we choose to take into account the convection via two different coefficients. T_∞ is the surrounding bulk temperature: $T_{\infty f}$ for the air in front of the lamps is higher than the one in the back $T_{\infty r}$. Consequently, we write the boundary conditions in the following way:

$$-k \nabla T \cdot \underline{n} = h_f (T - T_{\infty f}) \text{ on the face in front of the lamps;} \quad (17a)$$

$$-k \nabla T \cdot \underline{n} = h_r (T - T_{\infty r}) \text{ on the rear face} \quad (17b)$$

where h_f and h_r are the convective heat transfer coefficient on the face in front of the lamps and the one on the rear face.

The heat conductivity k , the specific mass ρ and the convective heat transfer coefficient h are assumed independent of temperature while the heat capacity C_p is considered as a function of the temperature, because heat capacity increases significantly with the temperature (see Fig. 5). According to the values referenced in Ref. [29], we propose the following function to represent the evolution of the specific capacity:

$$C_p = \Delta C_p \arctan(\alpha(T - T_g)) + C_{p1} \quad (18)$$

where ΔC_p is a constant related to the amplitude of the increased of the C_p value when passing from the glassy state to the rubber state, T_g is the more or less the glass transition temperature, C_{p1} is a specific capacity value corresponding to the glassy state of the material and α is a factor that fits the roughness of the jump of the curve.

Since the heat transfer is assumed as a 1D case which the temperature varies only in the thickness direction, the internal radiative intensity absorption \vec{q}_r is taken also as 1D and is managed by the Beer–Lambert law:

$$\vec{q}_r = \phi_{\lambda 0} e^{-k_\lambda s} \vec{z} \quad (19)$$

where: $\phi_{\lambda 0}$ is the incident radiation, k_λ is the spectral absorption coefficient of PET and s represent the path between the current position to the incident surface. From Fig. 8, s can be calculated as: $s = z - d$.

The heat equation (Eq. 16) with a nonlinear specific capacity (Eq. 18) and the equation of the internal heat flux (Eq. 19) are solved using a 1D finite element method. The implicit time integration scheme is chosen to solve this time-dependent problem. Due to the nonlinear specific capacity, a Newton–Raphson method is used to obtain the temperature field.

The Monte Carlo method is used to identify the parameters that best fit the experimental results. The domain of each parameter is defined from Ref. [29]. We generate the parameters randomly over the domain. On each draw, a computation is carried out and the numerical results are compared with the experimental temperatures. After drawing 10,000 random inputs, we obtain the parameters, with which the numerical results best matches the experimental data. The thermal properties are referenced in Table 3. This identification shows that h_f is smaller than the rear coefficient h_r . The specific mass ρ and the absorption coefficient k_λ have the same order of magnitude with reference. The heat conductivity k is smaller than the reference.

Figure 6 represents for each distance, the experimental temperature evolution on the surface in front of the lamps T_f (the blue one) and the one on the rear face T_r (the red one). With the identified parameters, the curves obtained have a substantially good representation of the experimental results (dots).

The evolution of C_p for PET Arnite D00301 is illustrated in Fig. 7, comparing with the one of material PET T4F9. They have the same order of magnitude except some differences at the lower temperature. The convective heat transfer coefficient h can be estimated from the relation proposed by Churchill and Chu [30]:

$$h = \frac{k}{L} \left(0.68 + \frac{0.67 R_a^{1/4}}{(1 + (0.492/P_r)^{9/16})^{4/9}} \right) \quad (20)$$

where L is the height of the sheet, R_a is the Rayleigh number, and P_r is the Prandtl number. $P_r = 0.688$ and $R_a = 1.6 \times 10^6$ when the temperature of PET reaches 100°C

TABLE 3. The value of thermal properties.

Parameter	ρ (kg m ⁻³)	C_p (J kg ⁻¹ K ⁻¹)				k (W m ⁻¹ K ⁻¹)	h (W m ⁻² K ⁻¹)		k_λ (m ⁻¹)
		C_{p1}	T_g	ΔC_p	α		h_f	h_r	
Value	1400	120	87	1650	0.1	0.07	7	16	$3 \cdot 10^4$

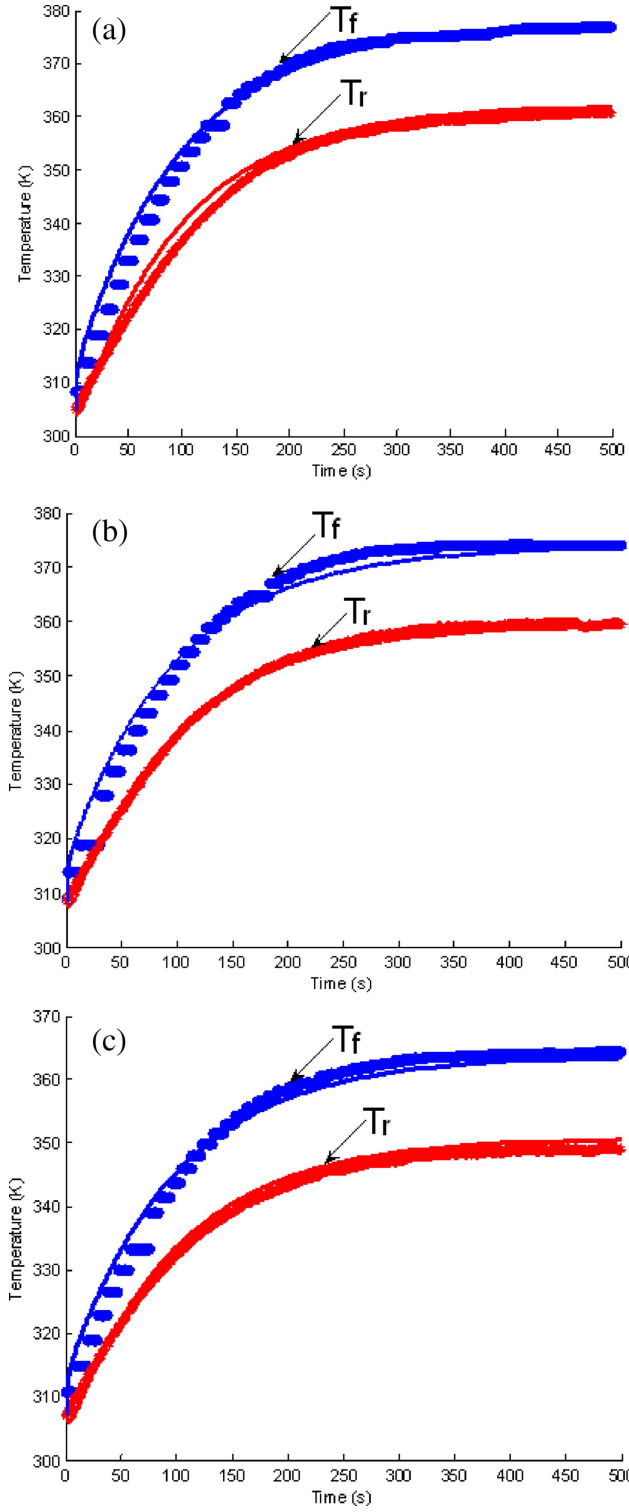


FIG. 6. The experimental results (dots) and the numerical results (curves) with optimal thermal properties: (a) $d = 11$ cm; (b) $d = 12$ cm; (c) $d = 13$ cm. [Color figure can be viewed in the online issue, which is available at [wileyonlinelibrary.com](#).]

[29], we can obtain the value of h using Eq. 20: $h = 11 \text{ W m}^{-2} \text{ K}^{-1}$. The identified h_r ($16 \text{ W m}^{-2} \text{ K}^{-1}$) is a little higher than this value estimated while h_f ($7 \text{ W m}^{-2} \text{ K}^{-1}$) is a bit lower than this one.

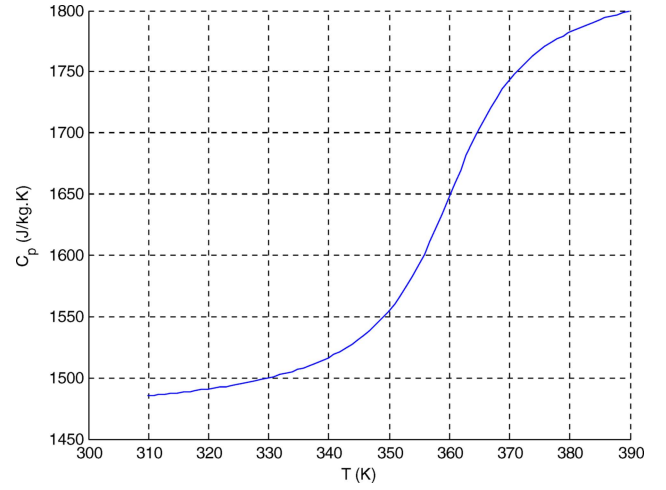


FIG. 7. The evolution of C_p with the parameters identified. [Color figure can be viewed in the online issue, which is available at [wileyonlinelibrary.com](#).]

Since we tested three different distances between the IR lamps and the PET sheet, the intensity of the incident radiation depends on the distance. In the following, we estimate this absorbed IR radiation $\phi_{\lambda 0}$ from a simple modeling based on the principle of spectral energy relation [29, 31]. Four identical IR lamps (radius $r = 2$ mm and length $l = 185$ mm) are modeled as cylinders separated by a distance $d_l = 15$ mm (Fig. 8b).

The amount of the radiation heat energy that comes from the surface element dA' at a collocation point M' ($x' = r \cos \varphi + h$, $y' = r \sin \varphi$) and reaches the surface element dA at a collocation point M ($x, y, z = d$) with the path vector \vec{w} (Fig. 8a), can be written in the following way:

$$dQ_{dA' \rightarrow dA} = \int_{\lambda_1}^{\lambda_2} \varepsilon_{\lambda} i_{\lambda}^b(\lambda) d\lambda \cdot \int_{\varphi=0}^{\varphi=\pi} \int_{y'=-l/2}^{y'=l/2} \cos \theta \cos \theta' \frac{dA}{\|M'M\|^2} \underbrace{dA'}_{rd\varphi dy'} \quad (21)$$

where λ is a given wavelength between 0.2 and $10 \mu\text{m}$ and ε_{λ} is the spectral tungsten emissivity equal to 0.26 [29]. The emissive power for a blackbody i_{λ}^b is given by Planck's law:

$$i_{\lambda}^b = \frac{2C_1}{\lambda^5 (e^{C_2/\lambda T_{\text{fil}}} - 1)} \quad (22)$$

where $C_1 \approx 1.19 \times 10^8 \text{ W m}^{-2} \mu\text{m}^4$, $C_2 \approx 14388 \mu\text{m K}$. We assume that the filament temperature is a uniform source at $T_{\text{fil}} = 1700 \text{ K}$. \vec{w} is a vector which represents the path of the radiation from M' to M :

$$\begin{aligned} \vec{w} &= \frac{\vec{M'M}}{\|M'M\|} = \frac{x - x'}{\|M'M\|} \vec{e}_x + \frac{y - y'}{\|M'M\|} \vec{e}_y + \frac{z - z'}{\|M'M\|} \vec{e}_z \\ &\approx \frac{x - h}{\|M'M\|} \vec{e}_x + \frac{y - y'}{\|M'M\|} \vec{e}_y + \frac{d}{\|M'M\|} \vec{e}_z. \end{aligned} \quad (23)$$

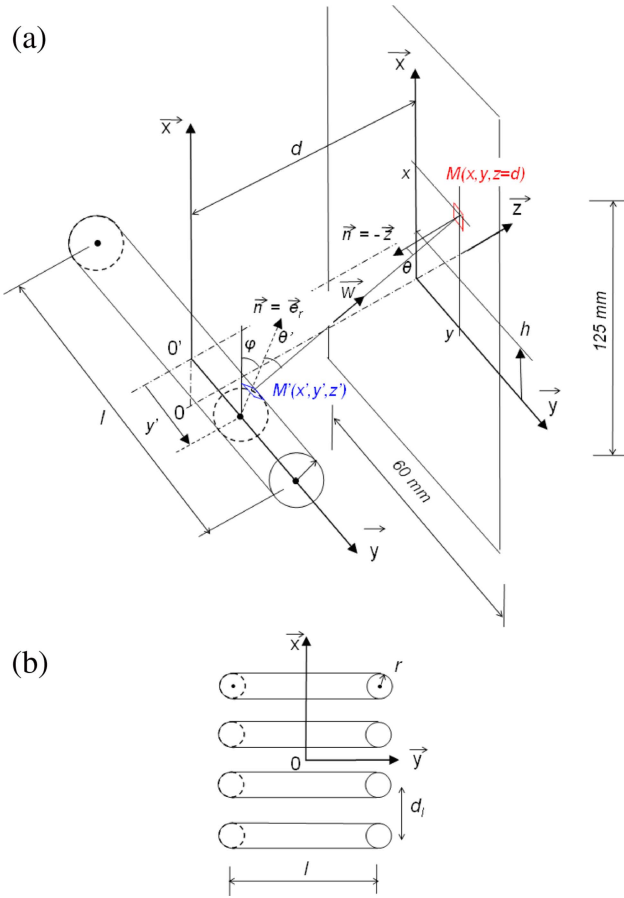


FIG. 8. (a) Geometrical configuration of the lamps and PET sheet; (b) position of the lamps. [Color figure can be viewed in the online issue, which is available at wileyonlinelibrary.com.]

The last approximation is related to the condition $r < d$. The two angles θ' and θ represent respectively, the angle between the normal at the lamp surface \vec{n}' at point M' and the path direction \vec{w} ; the angle between the normal at the PET sheet \vec{n} at point M and the path direction \vec{w} :

$$\cos \theta = \vec{w} \cdot \vec{e}_z \approx \frac{d}{\|M'M\|}, \quad \cos \theta' = \vec{w} \cdot \vec{e}_r \approx \frac{d}{\|M'M\|},$$

$$\cos \theta' = \vec{w} \cdot \vec{e}_r = \frac{(x-h) \cos \varphi}{\|M'M\|} + \frac{d \sin \varphi}{\|M'M\|} \quad (24)$$

where $\|M'M\| = \sqrt{(x-h)^2 + (y-y')^2 + d^2}$.

Once again, because the radius r is negligible compared to the distance d , Eq. 21 combining with Eq. 24 leads to:

$$dQ_{dA' \rightarrow dA} = \int_{\lambda_1}^{\lambda_2} \varepsilon_{\lambda} i_{\lambda}^b(\lambda) d\lambda \cdot 2\pi r d^2 \int_{y'=-l/2}^{y'=l/2} \frac{dA dy'}{\|M'M\|^2}. \quad (25)$$

Finally, the intensity per unit area of the incident radiation can be written as follow:

$$\phi_{\lambda 0}(M) = \frac{dQ_{\text{lamps} \rightarrow dA}}{dA}$$

$$= \int_{\lambda_1}^{\lambda_2} \varepsilon_{\lambda} i_{\lambda}^b(\lambda) d\lambda \cdot 2\pi r d^2 \sum_{i=1}^n \int_{y'=-l/2}^{y'=l/2} \frac{dy'}{\|M'M\|^2} \quad (26)$$

where $n = 4$ stands for four lamps.

We can see, from Fig. 9, that the intensity of the incident radiation reaching the PET sheet is not uniform. The maximum difference can reach 21% between the central zone of the PET sheet and the corners. Nevertheless, in the central region of study where the identification is done, the heterogeneity is less than 10% which validates the 1D approach used to manage the identification.

From Fig. 9d, one can also notice that the incident radiation $\phi_{\lambda 0}$ calculated in the central zone decreases with increasing distance. This value is close to the one identified from temperature measurements: both are listed in Table 4.

Implementation of the Heat Part of the Thermoviscohyperelastic Model

We consider a thermomechanical model to simulate the equibiaxial stretching of PET sheets to evaluate the self heating phenomenon. The mechanical part is shown in Eqs. 13–15. The weak form of the heat part can be written in the following way:

$$\begin{cases} \int_{\Omega} T^* \rho C_p \dot{T} d\Omega + k \int_{\Omega} \nabla T^* \cdot \nabla T d\Omega \\ = \int_{\Omega} T^* \left(\underline{\underline{\sigma}} : \underline{\underline{D}} \right) d\Omega - h \int_{\partial\Omega_q} T^* (T - T_{\infty}) dS. \quad (27) \\ T = T_0 \quad \text{at } t = 0 \end{cases}$$

$\partial\Omega_q$ is the union of the top and bottom face of the specimen. The process temperature is slightly above the temperature T_g . Under this condition, based on the evolution of the heat specific capacity C_p shown in Fig. 7, it can be assumed as constant ($1750 \text{ J kg}^{-1} \text{ K}^{-1}$). Because the sheet specimen is heated on both sides, the heat transfer coefficient h can be chosen equal to h_f ($7 \text{ W m}^{-2} \text{ K}^{-1}$). No thermal exchange is assumed between the specimen and the grips. To be consistent with the plane stress assumption, T is chosen as a function of the plane coordinates x, y and time (i.e., T is representative of the mean value of the temperature through the thickness e). Consequently, the weak form writes:

$$\begin{aligned} e \left(\rho C_p \int_{\partial\Omega} T^* \frac{\partial T}{\partial t} dS + k \int_{\partial\Omega} \nabla T^* \cdot \nabla T dS - \int_{\partial\Omega} T^* \left(\underline{\underline{\sigma}} : \underline{\underline{D}} \right) dS \right) \\ = 2 \int_{\partial\Omega_q} T^* (-h(T - T_{\infty})) dS \quad (28) \end{aligned}$$

where e is the thickness of the specimen. $\partial\Omega = \partial\Omega_q = S$ is the area of the 2D plane domain that represents the specimen. Since we assume that the thermal exchange only occurs on the top and bottom face of the PET sheet, the factor “2” before convective heat transfer term represents the total flux exchange from these two surfaces.

The dimension of the PET specimen during the test is $76 \text{ mm} \times 76 \text{ mm} \times 1.5 \text{ mm}$. The length and width are large with respect to thickness: $e < L$. Under this condition, the most convective heat exchange is on the top and bottom surfaces. The dissipated power density

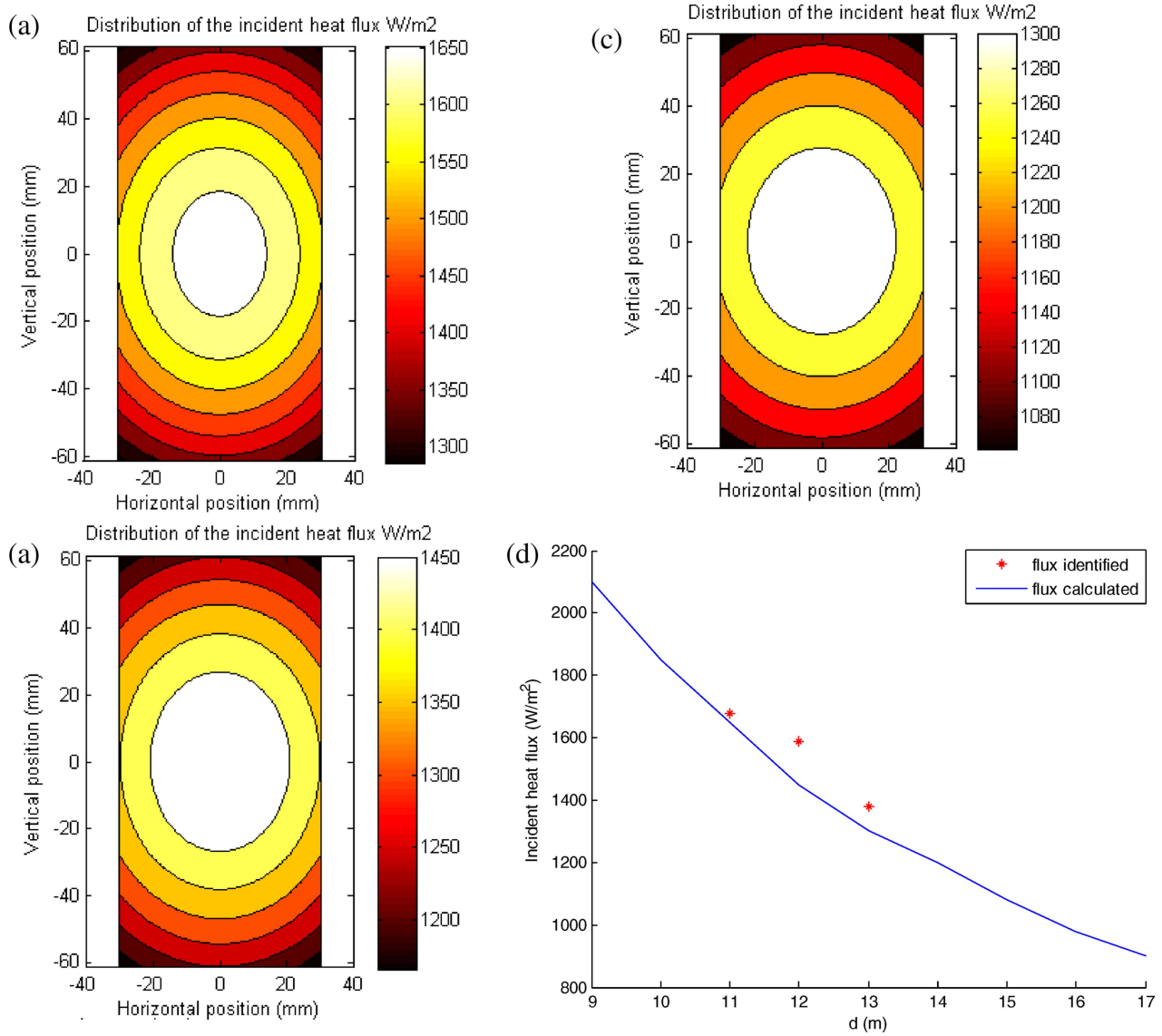


FIG. 9. The intensity of the incident radiation calculated by Eq. 26 (a) $d = 11$ cm; (b) $d = 12$ cm; (c) $d = 13$ cm. (d) The incident heat flux ϕ_{20} identified (the points) compared to ϕ_{20} calculated in the central zone (the line). [Color figure can be viewed in the online issue, which is available at wileyonlinelibrary.com.]

$\underline{\underline{\sigma}} : \underline{\underline{D}}$ is about 10^6 Pa s $^{-1}$ and is almost uniform in the specimen. This value leads to the Brinkman number B_r equals around 10:

$$B_r = \frac{\eta \bar{V}^2}{k(T_P - \bar{T})} \frac{e^2}{L^2}. \quad (29)$$

That means the viscous dissipation is 10 times larger than the heat conduction through the thickness.

TABLE 4. The values of incident heat flux.

D (cm)	11	12	13
ϕ_{20} calculated (W m $^{-2}$)	1650	1450	1300
ϕ_{20} identified (W m $^{-2}$)	1680	1590	1380

Furthermore, the biaxial stretching process is considered fast enough in regard of the time needed to propagate the temperature through the thickness. The characteristic time for diffusion is $t_d = \rho C_p e^2 / k = 57$ s and the characteristic time for capacity is $t_c = \rho C_p e / h = 132$ s. The time for the process is about 2 s. If we compare the mean value of the temperature through the thickness $\bar{T} = \bar{T}(x, y, t)$ in the plane stress case with the $T(x, y, z, t)$ in the axisymmetric case, the difference between the mean value of the temperature \bar{T} obtained by Eq. 28 and the temperature T calculated from the weak form with the definite integral over the thickness is nearly 0.55°C . This difference causes an error on viscosity that is less than 3%. Therefore, in the following, we use Eq. 28 to simulate the thermal part.

Optimization of the Mechanical Parameters of the Thermoviscohyperelastic Model

Mechanical and thermal balance equations are fully nonlinear and solved together with implicit schemes on the current deformed configuration, which is updated at each time step. The thermal parameters are identified from the experimental IR heating and the mechanical ones are identified from the assuming isothermal equibiaxial elongation. Both are listed in Tables 2 and 3.

We implement the thermal part in the finite element approach together with the mechanical part. Therefore, three fields (global velocity V , elastic left Cauchy Green tensor B , and temperature T) formulation has been performed. We choose the linear interpolation for temperature. Equations 13–15 that solve only the mechanical part has to also add the heat equations. The Newton–Raphson residual for the heat part is:

$$R_T = \rho C_p \int_{\partial\Omega} T^* \frac{\partial T}{\partial t} dS + k \int_{\partial\Omega} \nabla T^* \nabla T dS - \int_{\partial\Omega} T^* (\underline{\underline{\sigma}} : \underline{\underline{D}}) dS - \frac{2}{e} \int_{\partial\Omega_q} T^* (-h(T - T_\infty)) dS. \quad (30)$$

The consistent linearization leads to the linear form of this problem for the increment ΔV , ΔB_e , and ΔT which can be given in the following way:

$$\begin{bmatrix} [D_{\Delta V}\{R_V\}] & [D_{\Delta B_e}\{R_V\}] & [0] \\ [D_{\Delta V}\{R_{B_e}\}] & [D_{\Delta B_e}\{R_{B_e}\}] & [D_{\Delta T}\{R_{B_e}\}] \\ [D_{\Delta V}\{R_T\}] & [0] & [D_{\Delta T}\{R_T\}] \end{bmatrix} \begin{Bmatrix} [\Delta V] \\ [\Delta B_e] \\ [\Delta T] \end{Bmatrix} = - \begin{Bmatrix} [R_V] \\ [R_{B_e}] \\ [R_T] \end{Bmatrix}. \quad (31)$$

The adding Gateaux derivatives of nonlinear operator corresponding to the residuals (R_V , R_B and R_T) can be written:

$$\begin{aligned} D_{\Delta T}\{R_B\} &= \int_{\Omega} \underline{\underline{B_e}}^* : G(\underline{\underline{\varepsilon_e}}) \underline{\underline{B_e}} \underline{\underline{\hat{B_e}}} D_{\Delta T} \left\{ \frac{1}{\eta(\underline{\underline{\varepsilon_v}}, \underline{\underline{\hat{\varepsilon_v}}}, T)} \right\} d\Omega \\ D_{\Delta V}\{R_T\} &= - \int_{\Omega} T^* (\underline{\underline{\sigma}} : \Delta \underline{\underline{D}}) d\Omega \\ D_{\Delta T}\{R_T\} &= \int_{\Omega} T^* \rho C_p \Delta \dot{T} d\Omega + k \int_{\Omega} \nabla T^* \nabla (\Delta T) d\Omega. \end{aligned} \quad (32)$$

Figure 10 shows that stresses obtained from this thermomechanical simulation are lower than the experimental data. Because the temperature increases during the biaxial elongation, the self-heating effect affects the mechanical properties, especially the viscosity which decreases. Consequently, the parameters identified assuming an isothermal elongation must be modified to take into account this.

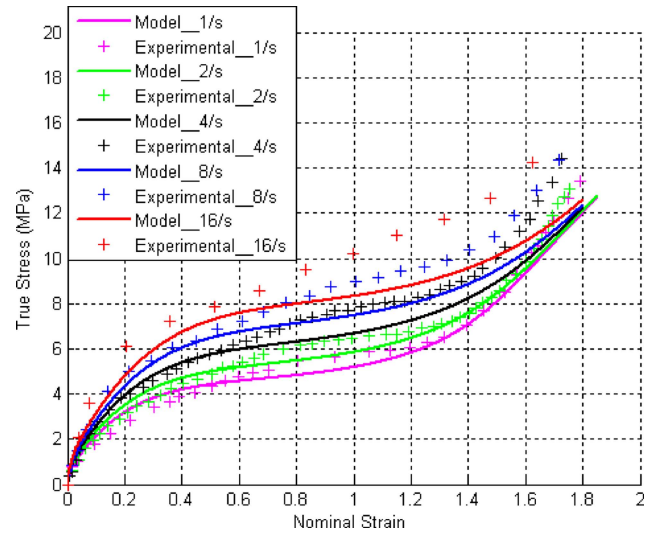


FIG. 10. The experimental data (the points) and the thermomechanical results. [Color figure can be viewed in the online issue, which is available at wileyonlinelibrary.com.]

As the self-heating effect is not negligible and produces an important effect on the viscous part of the model, the first estimation of the parameters obtained from our isothermal identification must be adjusted.

The parameters in the viscosity $\eta(\underline{\underline{\varepsilon_v}}, \underline{\underline{\hat{\varepsilon_v}}}, T)$ are needed to optimize. The purpose is to minimize the mean difference between the experimental results and the numerical ones. The function “fminunc” in the Matlab Optimization Toolbox is then chosen for the optimization procedure. The characteristics identified from the isothermal elongation in Table 2 are applied as the starting point of each parameter. Finally, the characteristics of the PET for these viscohyperelastic model expressions to represent conveniently the biaxial experimental tension tests are listed in Table 5.

Comparing with the values of Table 2, one can observe that only the values of the WLF-like coefficients are influenced by this adjustment. Other coefficients that appear in the mechanical part of the model vary very few: the initial identification makes finally sense even if an adjustment is needed a posteriori.

RESULTS

With these parameters identified from the optimization, we can obtain the stress–strain curves from the thermoviscohyperelastic model. Figure 11 shows the comparison

TABLE 5. The characteristics of the PET.

$G_0 = 8 \text{ MPa}$	$\eta_0 = 9 \text{ MPa}\cdot\text{s}$	$C_1 = 0.88$
$\Lambda = 0.001$	$K = 3$	$C_2 = 105.8^\circ\text{C}$
$\lambda = 10.51$	$h_0 = -0.21$	$B_1 = 0.07$
$a = 2$	$N = 0.3$	$B_2 = 180.8^\circ\text{C}$
$m = 0.23$	$\varepsilon_{vlim_ref} = 1.43$	

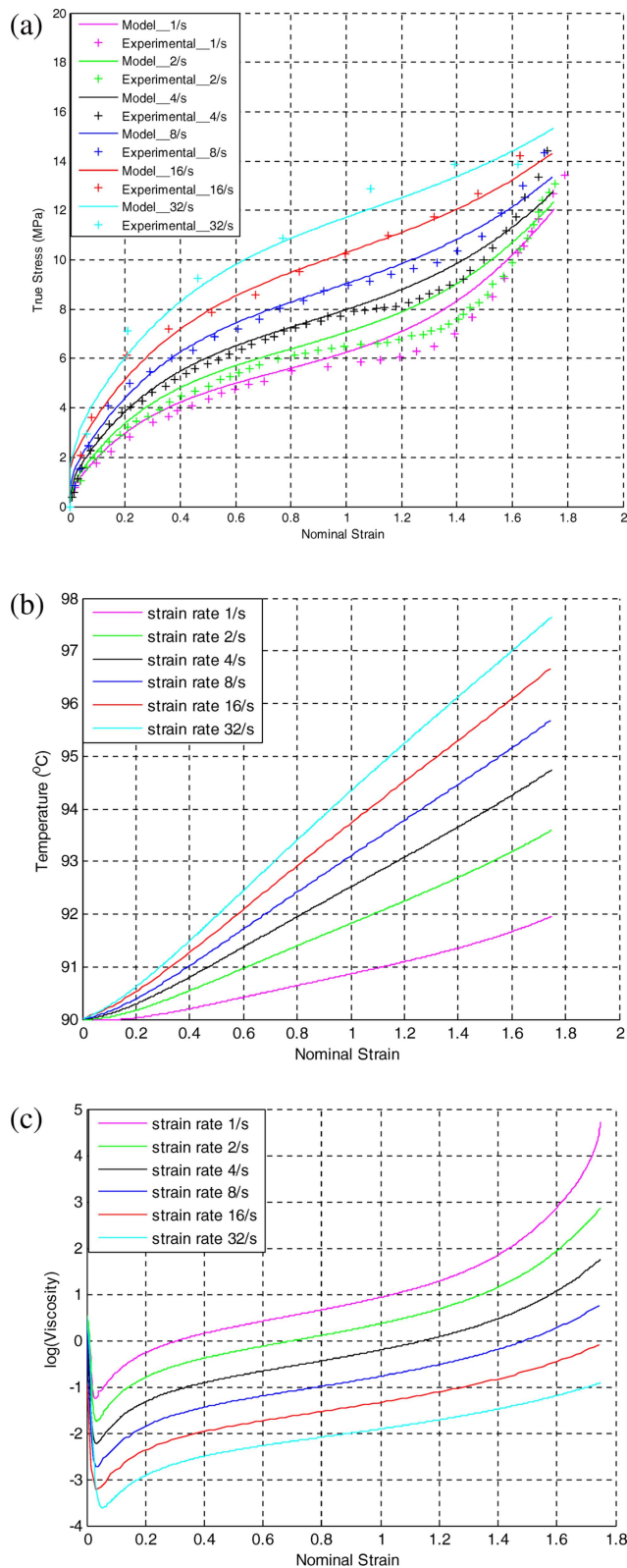


FIG. 11. (a) The experimental data (the points) and the thermomechanical results; (b) the evolution of temperature under different strain rates; (c) the calculated evolution of the viscosity under different strain rates during the biaxial test including the temperature effect. [Color figure can be viewed in the online issue, which is available at wileyonlinelibrary.com.]

TABLE 6. Errors between the experimental and the results of the model.

Strain rate (s^{-1})	Relative error (%)
1	6.72
2	8.4
4	4.97
8	4.45
16	8.55
32	9.25

between the stresses obtained from this thermomechanical simulation and from the experimental data. The mean difference does not exceed 10% for each deformation rate showed in Table 6.

We can notice that the increasing evolution of the temperature versus strain is nearly linear. The increase in the temperature is the same order of magnitude but little lower than the one observed in the experimental test presented in [17]. Furthermore, the self-heating of the specimen increases regularly for strain rates varying from 1 to $32 s^{-1}$ where the temperature increases nearly of $6^{\circ}C$ (see Fig. 11b). It confirms that at very high deformation rate observed during ISBM process, the adiabatic heating due to the viscous dissipation may generate a significant temperature rises.

We can see in the Fig. 11c, the effect of temperature on the viscosity evolution. For example, the final slope of the viscosity curve for the strain rate $32 s^{-1}$ is much lower than the one for lower strain rates; therefore, the strain hardening effect is not so considerable at $32 s^{-1}$.

If we examine the high strain rate case, for example, at $32 s^{-1}$ for $90^{\circ}C$, the coupled themoviscohyperelastique model simulation gives the stress evolution plotted in Fig. 11a which have 9.25% errors with the experimental data.

One can see that the stress evolution measured during the experiment saturates and does not increase as the lower strain rate case when approaching the 1.8 elongation. This may be explained by the higher temperature level coming from the self-heating of the specimen for this test. Our model does not predict the decreasing shape but gives a pretty good estimation on the evolution with nearly no strain hardening effect for this case.

CONCLUSIONS

A viscohyperelastic model identified from the equibiaxial tests performed at conditions close to ISBM process strain rate and temperature was implemented for numerical simulations. This finite elements model was used to simulate the plane stress test. It reproduces successfully the experimental results and can be used to simulate uniaxial or sequential biaxial tests to predict the PET behavior for isothermal conditions.

Experiments have been conducted to characterize the thermal properties of the PET in the range of the ISBM temperature. Thermal imaging has been used to determine the surface temperature distribution of the PET sheets which are heated by IR lamps. The Monte Carlo method is used to provide the parameters best fit the temperature evolution. Comparison between the obtained values and values coming from the literature, especially for the IR heating radiation flux, validates the identification approach.

The coupled thermoviscohyperelastic model proposed has been used to manage a finite element simulation of the equibiaxial elongation test. The weak form of the model has been implemented in Matlab. It shows that the thermal effects have an important influence on the viscous part of the model and WLF-like parameters have to be adjusted by nonisothermal simulations. With the adjusted parameters, we obtained: (i) that stress–strain curves from this thermoviscohyperelastic model fit well with the experimental data; (ii) that self-heating of the specimen is not negligible and can reach nearly 10°C for the highest strain rate which is conform (slightly lower) to the temperature measurements made on the specimen.

In further works, we intend to implement an axisymmetric version of the viscohyperelastic model coupled to temperature to simulate accurately the ISBM process.

ACKNOWLEDGMENTS

This work could not be possible without IR lamps given by Sidel Company and without injection of the PET sheets made by the LIM at Arts et Métiers ParisTech. Special thanks to G. Menary of QUB for his experimental study from which the identification has been possible.

REFERENCES

1. G. Marckmann, E. Verron, and B. Peseux, *Polym. Eng. Sci.*, **41**(3), 426 (2001).
2. E. Gorlier, J.F. Agassant, J.M. Haudin, and N. Billon, *Plast. Rubber Compos. Process. Appl.*, **30**(2), 48 (2001).
3. E. Gorlier, J.M. Haudin, J.F. Agassant, J.L. Lepage, G. Perez, D. Darras, and N. Billon, *The 14th International ESAFORM Conference on Material Forming*, Liège, 345 (2001).
4. L. Chevalier and Y. Marco, *Int. J. Mech. Mater.*, **39**(6), 596 (2006).
5. M. Bordival, F.M. Schmidt, Y. Le Maout, and V. Velay, *Polym. Eng. Sci.*, **49**(4), 783 (2009).
6. B. Cosson, L. Chevalier, and J. Yvonnet, *Int. Polym. Process.*, **24**(3), 223 (2009).
7. L. Chevalier, Y. Marco, and G. Regnier, *Mec. Ind.*, **2**, 229 (2001).
8. F.M. Schmidt, J.F. Agassant, M. Bellet, and L. Desoutter, *J. Non-Newt. Fluid Mech.*, **64**(1), 19 (1996).
9. G. Barakos and E. Mitsoulis, *J. Non-Newt. Fluid Mech.*, **58**, 315 (1995).
10. B. Debbaut, B. Hocq, and J. M. Marchal, *SPEANTEC Tech. Papers*, **39**, 1870 (1993).
11. C.P. Buckley and D.C. Jones, *Polymer*, **36**, 3301 (1995).
12. C.P. Buckley, D.C. Jones, and D.P. Jones, *Polymer*, **37**, 2403 (1996).
13. G.H. Menary, C.G. Armstrong, R.J. Crawford, and J.P. McEvoy, *Rubber Compos. Process. Appl.*, **29**, 360 (2000).
14. L. Figiel and C.P. Buckley, *Int. J. Non-Linear Mech.*, **44**, 389 (2009).
15. Y.M. Luo, L. Chevalier, and E. Monteiro, *The 14th International ESAFORM Conference on Material Forming*, Queen's University, Belfast, Ireland du Nord, April 27–29 (2011).
16. L. Chevalier, Y.M. Luo, E. Monteiro, and G. Menary, *Mech. Mater.*, **52**, 103 (2012).
17. G.H. Menary, C.W. Tan, E.M.A. Harkin-Jones, C.G. Armstrong, and P.J. Martin, *Polym. Eng. Sci.*, **52**(3), 671 (2012).
18. K. Chung, *J. Mater. Shaping Technol.*, **7**(4), 229 (1989).
19. F.M. Schmidt, J.F. Agassant, and M. Bellet, *Polym. Eng. Sci.*, **38**(9), 1399 (1998).
20. Z.J. Yang, E. Harkin-Jones, G.H. Menary, and C.G. Armstrong, *Polym. Eng. Sci.*, **44**, 1379 (2004).
21. Z.J. Yang, E. Harkin-Jones, G.H. Menary, and C.G. Armstrong, *J. Mater. Process. Technol.*, **153**(154), 20 (2004).
22. F.M. Schmidt, Y. Le Maout, and S. Monteix, *J. Mater. Process. Technol.*, **143**(144), 225 (2003).
23. S. Andrieu, *Etude expérimentale et numérique du chauffage infrarouge de plaques thermoplastiques pour le thermoformage*, Thèse de Doctorat, ENSMP (2005).
24. F. Brezzi and M. Fortin, *Mixed and hybrid Finite Element Methods*, Springer, New York (1991).
25. R. Siegel and J.R. Howell, *Thermal Radiation Heat Transfer*, 3rd ed., Hemisphere Publishing Corporation (1992).
26. F.M. Schmidt, Y. Le Maout, and S. Monteix, *J. Mater. Process. Technol.*, **143**(144), 225 (2003).
27. B. Cosson, F. Schmidt, Y. Le Maout, and M. Bordival, *Int. J. Mater. Form.*, **4**, 1 (2011).
28. J. Sacadura, *Initiation Aux Transferts Thermiques*. Lavoisier, France (1973).
29. M. Bordival, *Modélisation et optimisation numérique de l'étape de chauffage infrarouge pour la fabrication de bouteilles en PET par injection-soufflage*, Thèse de doctorat, Mines Tech Paris (2009).
30. S.W. Churchill and H.S. Chu, *Int. J. Heat Mass Transfer*, **18**, 1323 (1975).
31. M.F. Modest, *Radiative Heat Transfer*, 2nd ed., McGraw-Hill, Inc., New York (1993).